An investigation of internal flame structure in porous media combustion via X-ray Computed Tomography

Jared Dunnmon [a,*], Sadaf Sobhani [a], Meng Wu [b], Rebecca Fahrig [b], Matthias Ihme [a]

[a] *Department of Mechanical Engineering, Stanford University, Stanford, CA 94305-3024, United States*
[b] *Department of Radiology, Stanford University, Stanford, CA 94305-3024, United States*

Abstract

X-ray Computed Tomography (XCT) measurements are performed to characterize the internal volumetric flame structure within a Porous Media Burner (PMB). X-ray attenuation measurements are obtained using a multi-zone silicon carbide PMB combusting a radiodense $Kr/O_2/N_2/CH_4$ mixture designed to enhance X-ray contrast. Time-averaged tomographic reconstructions of the X-ray attenuation field are used to assess internal PMB flame structure. Several key internal physical phenomena are observed, including heat recirculation within the combustion region, spatial inhomogeneity within the reaction zone, and preheating of gas in the upstream porous section. Further, the theory of XCT measurements applied to combustion systems is developed and implemented to arrive at 3D implied temperature field measurements at high spatial resolution. Implied temperature results are shown to exhibit quantitative agreement with those of a known 1D volume-averaged model for porous media combustion as well as with standard thermocouple measurements. These results shed light on internal thermophysical processes within PMBs while demonstrating the significant potential of XCT in obtaining quantitative, spatially resolved field data within optically inaccessible combustion environments.

© 2016 The Combustion Institute. Published by Elsevier Inc. All rights reserved.

Keywords: Porous media combustion; X-ray Computed Tomography; Heterogeneous combustion; Combustion diagnostics; Volume-averaged modeling

1. Introduction

Porous Media Burners (PMBs) facilitate combustion of a gas mixture within the voids of a solid matrix, which results in chemical and physical char-

acteristics different than those observed in conventional, purely gas-phase combustion systems. The flame is stabilized inside the porous material, where the superior thermal conductivity and radiation properties of the solid compared to those of the gas mixture alone result in higher consumption rates and enhanced heat transfer, leading to lower nitrogen oxide (NO_x) emissions. Furthermore, the large interfacial surface area of the porous matrix and its

---

* Corresponding author.

E-mail addresses: jdunnmon@stanford.edu (J. Dunnmon), mihme@stanford.edu (M. Ihme).

high heat capacity provide enhanced combustion stability [1]. Due to these favorable properties, interest in porous media combustion technology has continued to advance. PMBs can serve as a more efficient, robust, and environmentally friendly alternative for a wide variety of current combustion systems. Such applications include surface heaters, domestic heating units, reformers, and afterburners in solid oxide fuel cells [2].

In this work, we utilize an extension of the two-zone PMB design first proposed by Trimis and Durst [1], in which stability is achieved via pore-scale quenching as governed by a critical Peclet number [3]. Using this two-zone porous burner design, Khanna et al. [4] successfully demonstrated that PMBs are characterized by particularly low CO and NO_x emissions when compared to free-flame systems. Barra et al. [5] complemented this work by performing a numerical investigation of the optimal conditions for flame stabilization in the two-zone burner design, in which it was found that the heat conductivity and volumetric heat transfer coefficient of the solid structure are critical in determining heat re-circulation levels and stability boundaries. Using a 1D time-dependent formulation with detailed reaction chemistry, Barra and El-lzey later showed that the heat re-circulation efficiency decreases with increasing equivalence ratio, and that the heat transfer properties were primarily independent of the burner length [6].

While understanding of porous media combustion has clearly improved over recent decades to the point that several designs have been suggested for highly stable PMBs, we still lack an adequate fundamental understanding of detailed physical processes and internal flame structure inside the porous media. Current experimental methods applicable to PMBs generally encounter several limitations, but are primarily hindered by the opaque solid structure obscuring the flame region. Common methods include pointwise temperature measurements from thermocouples and analysis of exhaust gas composition [7]. Difficulties in optical access inhibit the use of several experimental tools such as Coherent Anti-Stokes Raman Spectroscopy (CARS), Particle Image Velocimetry (PIV), and Planar Laser-Induced Fluorescence (PLIF). Engineered access for optical techniques such as CARS [8] and PLIF [9] have been successful in obtaining useful data inside operating PMBs, but these techniques do not yield high-resolution volumetric visualization of flame structure or 3D field data. To address these challenges, we pursue the use of X-ray Computed Tomography (XCT) technology as an alternative experimental diagnostic that enables interrogation of the heterogeneous combustion processes within PMBs.

We proceed by first giving a brief overview of the theory behind application of XCT to combustion systems in Section 2 before describing the set of experiments used to test these ideas in Section 3. Key details of data analysis are discussed in Section 4 while important results are presented and analyzed to draw useful conclusions about this PMB system in Section 5.

2. Theory of XCT as a combustion diagnostic

XCT methods are being applied to fluid mechanics problems with increasing frequency, particularly in the context of multiphase flows and fuel sprays [10,11]. While applications to multiphase flows are a natural extension of traditional XCT uses in separating solids, liquids, and gases based on density differences, recent work has extended these methods to quantitatively describe gas-phase scalar transport. Specifically, it has been shown that XCT can be used to create quantitative 3D datasets describing the mole fraction of krypton, a radio-dense tracer gas, at energies characteristic of clinical and research scanners [12]. The interaction between X-ray photons and an object scanned with a monochromatic (single-energy) X-ray beam follows the Beer–Lambert law,

$$\ln\left(\frac{N_d}{N_0}\right) = - \int \mu(s)ds, \tag{1}$$

where N_0 is the incident X-ray photon count, N_d is the detected X-ray photon count, s is the path length through the object, and μ is the linear attenuation coefficient of the object. XCT measurements allow for reconstruction of the attenuation field in three spatial dimensions from a set of projections taken over a large number of angles [13]. The linear attenuation coefficient may be expressed in terms of the mass attenuation coefficient ξ and the density ρ of the material,

$$\mu = \xi\rho, \tag{2}$$

where ξ is a nonlinear function of the photon energy that varies with material composition. Note that ξ is most fundamentally an atomic quantity that increases with electron density, and can be determined via measurements of both μ and ρ at reference conditions [13,14]. Values of the mass attenuation coefficient depend on X-ray photon energies, and most X-ray sources emit a polyenergetic photon spectrum. Thus, one needs to supply an effective spectrally averaged mass attenuation coefficient $\bar{\xi}$ in order to use Eq. (1). We will refer to spectrally averaged quantities throughout this manuscript with an overbar.

Writing Eq. (2) for a mixture of gases and introducing the partial density ρ_j gives,

$$\bar{\mu} = \sum_{j=1}^{N} \bar{\xi}_j \rho_j = \frac{P}{R_u T} \sum_{j=1}^{N} \bar{\xi}_j X_j W_j, \tag{3}$$

taking P as pressure, W_j as the molar mass of species j, R_u as the universal gas constant, and X_j

as the mole fraction. In the case of a radiodense tracer gas such as krypton combined with low-$\bar{\xi}$ gases, one may treat Eq. (3) as the combination of attenuation from the tracer and from the balance of the system. In this case, one may extend Eq. (3) to yield the following simple expression for gas temperature in terms of known and measured quantities,

$$T = \frac{PW_{Kr}X_{Kr}\bar{\xi}_{Kr}}{R_u \Delta \bar{\mu}}, \qquad (4)$$

where $\Delta \bar{\mu} = \bar{\mu}_M - \bar{\mu}_B$, $\bar{\mu}_B$ is the attenuation measured in a background scan (with only non-attenuating species in the burner), and $\bar{\mu}_M$ is the attenuation of the burner containing a krypton-augmented gas mixture. Because atomically light gases such as combustion products and ambient air effectively do not attenuate, the $\bar{\mu}_B$ value is a good measurement of the appropriate signal to be subtracted to isolate the attenuation resultant from the radiodense tracer [12].

A final aspect of XCT theory that is crucial to the application of the technique to combustion systems relates to how Signal-to-Noise Ratio (SNR) is affected by various physical parameters. The analysis of Macovski [13] yields the following relation for SNR of XCT data obtained in a non-attenuating background medium such as air,

$$SNR = \frac{\Delta \bar{\mu}}{\sigma_\mu} \propto \Delta \bar{\mu} \sqrt{\bar{N} M} \propto \Delta \bar{\mu} \sqrt{MI_T w^2 \tau}, \qquad (5)$$

where σ_μ is the standard deviation of the attenuation measurements, $\bar{N}$ is the average photon count per detector pixel measurement, M is the number of projections contributing to the reconstruction, I_T is the tube current, w is the detector pixel width, and τ is the projection exposure time [15].

Combining Eqs. (4) and (5) and assuming that one averages over n different reconstructions to improve SNR yields the following expression relating expected noise levels to both scan parameters and physical state variables,

$$SNR \propto \frac{PW_{Kr}X_{Kr}\bar{\xi}_{Kr}}{R_u T} \sqrt{MI_T w^2 \tau n}. \qquad (6)$$

This equation shows that any physical change that increases the number density of krypton atoms in the flow will increase SNR – this includes pressure increases, temperature decreases and krypton mole fraction increases. In addition, increasing tube current, effective pixel size, exposure time, number of reconstructions averaged over, and number of projections per reconstruction further increase SNR. Considering the effects of each of these variables on overall measurement quality will be critical in designing effective combustion experiments utilizing XCT diagnostics.

3. Experimental setup and procedure

3.1. Burner setup

Figure 1 shows the porous burner and the experimental setup of the XCT that was utilized in this study. A three-stage porous burner emplacement (Fig. 1(a)) was constructed such that the flame stabilization point would be directly in the field of view of the X-ray detector, as shown in Fig. 1(b). The burner consisted of a quartz tube (Western Industrial Ceramics) of 0.41 cm thickness, 5.59 cm inner diameter, and 17.78 cm length surrounding three adjacently placed Silicon Carbide (SiC) disks (Ultramet) of 2.54 cm in height and 5.08 cm in diameter. A fine-pore 100 Pores-Per-Inch (PPI) disk was placed furthest upstream for use as a flashback arrestor and flow homogenizer, followed by a 65 PPI disk for flame quenching and a 3 PPI disk that functioned as the combustion zone. SiC disks were held in place via a compression fit using a ceramic fiber insulation lining (Western Industrial Ceramics). Note that the lowest disk was placed 2.5 cm above the quartz tube inlet in order to leave a substantial region wherein the unburned gas could be imaged for calibration purposes. Gases were supplied from compressed gas cylinders outfitted with dual-stage regulators (Prostar) to ensure a constant pressure supply. A radiodense four-component $Kr/N_2/O_2/CH_4$ mixture was combusted at lean conditions within the PMB. Component gases in the premixed stream were combined using a set of tee junctions, and each gas line was instrumented with a check valve to further protect against potential flashback. Flow rates were controlled and measured using a set of rotameters for each constituent gas. Rotameter accuracy was $\pm 5\%$ for methane and $\pm 3\%$ for all other gases.

Mixing occurred in a tube of 40 cm in length directly preceding the vertical burner emplacement, which consisted of a rotary union (DSTI), flashback arrestor (Superflash), burner mount, and burner body. The burner was secured to a precision rotary motor (Parker) by bolting the bottom lip of the quartz tube between two aluminum disks padded with ceramic fiber insulation. This assembly was supported on the motor via an aluminum plate augmented with a pipe connection at its center. This plate was preceded by the flashback arrestor and rotary union that respectively ensured no flame propagation back into the mixing system and allowed for well-controlled rotation of the burner by the XCT motor without gas leakage. Such a setup is necessary to perform tabletop XCT of combustion systems because obtaining projections at very precise angles is critical for faithful XCT reconstruction.

3.2. XCT-scanner and scan parameters

All experiments were performed on the tabletop X-ray radiography system shown in Fig. 1(b) using
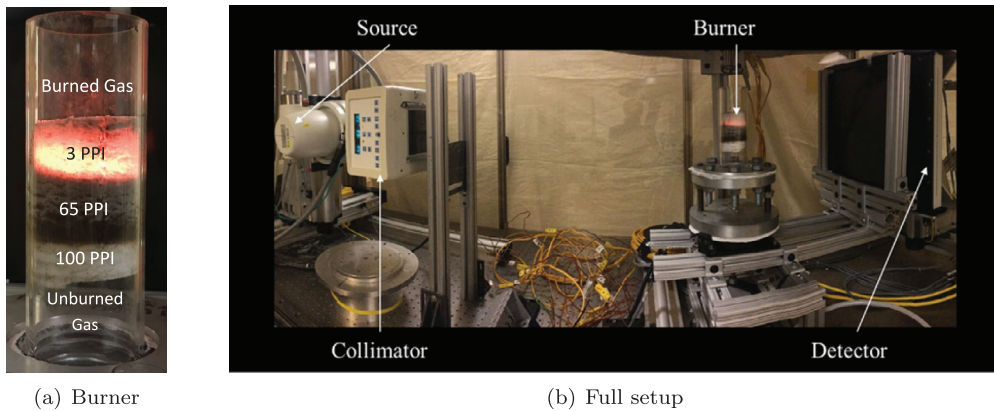
(a) Burner (b) Full setup

Fig. 1. Experimental setup, showing (a) burner setup and (b) XCT-system.

a fluoroscopic X-ray source and a flat panel detector with pixel spacing of 0.338 mm. A CPI Indico 100 fluoroscopic X-ray source was utilized along with a Huestis Model 150A collimator. X-ray signals were collected using a Varian Model 4030B detector with a cesium-iodide scintillator and amorphous silicon type n-i-p photodiodes. As shown in Fig. 1(b), the burner is placed between the source-collimator assembly (left) and detector (right) on a precision rotating table (Parker) to acquire 1200 projections over 360°. In this experiment the highest allowable projection number was used to maximize SNR.

Source-to-isocenter distance was 944.8 mm and source-to-detector distance was measured at 1255.5 mm. Scans were conducted with a 60 kVp and 50 mA X-ray beam to maximize SNR. As implied by Eq. (6), the tube current was set as high as possible without saturating the detector, and the energy level was chosen to be as low as possible while maintaining viably high photon counts. The 3D reconstruction volume is $384 \times 384 \times 700$ voxels in size with 200 μm isotropic spacing. Polynomial beam hardening correction for the outer quartz material was performed in the projection domain [16]. The 3D images were reconstructed using the Feldkamp-Davis-Kress (FDK) method with a Hamming windowed ramp kernel to eliminate high-frequency noise [15].

3.3. Experimental procedure

Before proceeding to obtain tomographic data describing the operational burner, calibration scans were performed at ten different X_{Kr} values inside the quartz tube in order to confirm that measured absorbance, defined by Eq. (1), was indeed linear in krypton number density (as measured by mole fraction at ambient conditions). Importantly, the relation between absorbance and krypton number density is independent of whether number density changes via temperature (with constant pressure

and krypton mole fraction) or X_{Kr} (with constant pressure and temperature).

Following the success of this initial calibration, a steady flow of premixed gas was established through the burner with a mixture of $X_{Kr} = 0.375$, $X_{N_2} = 0.368$, $X_{O_2} = 0.192$, and $X_{CH_4} = 0.065$ at a linear bulk velocity of 3.8 cm/s, overall flow rate of 4.6 SLPM, and nominal equivalence ratio of $\Phi = 0.69$. This flow was created by mixing three gas streams: an 80% Kr – 20% O_2 mixture, methane, and air. Given these conditions, we compute a pore-scale Reynolds number on the order of $Re_P = 5$, which is well within the laminar regime. We therefore expect this flame to behave in laminar fashion throughout the course of the experiment. Finally, the flame was ignited at the outlet using a small torch, at which point the flame would travel upstream within the quartz tube and eventually settle at the 3 PPI – 65 PPI interface.

The gas composition utilized here was chosen in order to obtain reasonable X-ray contrast while mitigating the effect of the krypton tracer on combustion chemistry and heat transfer. Further, as implied by Eq. (6), one could conceivably achieve similar SNR with the same spatial resolution and sample size using a mixture with even smaller X_{Kr} by utilizing an XCT system that allows for higher tube currents, a larger number of projections, or longer exposure times. Each of these improvements is certainly achievable in general, but all were beyond the capability of the specific system utilized in this study. To demonstrate the applicability of these recommendations, we performed a simple experiment wherein a single reconstruction of the burner phantom filled entirely with krypton gas was performed using data acquired at both $I_T = 20$ mA and $I_T = 50$ mA. Based on Eq. (6), one would expect an SNR ratio of $SNR_{50}/SNR_{20} = \sqrt{50/20} = 1.58$. The actual value calculated from the experiment in a region above the 3 PPI porous media was $SNR_{50}/SNR_{20} = 1.59$. This result supports the validity of the scaling analysis contained in Eq. (6),

and implies that even lower krypton concentrations could be used. For instance, simply utilizing a common clinical X-ray source with characteristic tube current of at least 200 mA would allow for a 50% SNR increase over the system used here at the same photon energy—this would enable results similar to those shown here to be obtained with an X_{Kr} value half of that used in the current experiment.

Once a flame was established, a set of detailed temperature measurements were conducted within the burner using a set of five type-K thermocouples mounted radially above the burner exit with 5 mm spacing in the radial direction. The thermocouple assembly was mounted on a vertical track to allow for axial temperature traverses — these temperature data taken from the burned gas will be used to provide validation for the implied temperature field extracted from XCT measurements.

Our goal in the tomographic data acquisition is to obtain subtracted measurements of $\Delta\bar{\mu} = \bar{\mu}_M - \bar{\mu}_B$. Thus, after preheating the X-ray tube to ensure flux stability, we first perform twenty tomographic acquisitions of the burner combusting the Kr/N₂/O₂/CH₄ mixture at steady-state to obtain measurements of $\bar{\mu}_M$. Flame stability was confirmed over the duration of the experiment both visually (as in Fig. 1(a), flame radiation is visible through the burner insulation) and indirectly with thermocouples situated above the outlet of the quartz tube (so as not to cause X-ray scattering in the burner tube). Each tomographic acquisition involved a 360° rotation of the burner occurring over a period of one minute, and each full scan cycle required eight minutes to perform tomographic acquisition, execute detector offset calibration for the next scan, and ensure that the X-ray tube was at a consistent thermal state at the start of each scan. After these twenty scans of the burning radiodense mixture were recorded, the krypton-containing gases were removed from the gas stream and replaced with an air flow such that the same amount of fuel continued to combust at the interface, but with no radiodense tracer in the premixed gas. Twenty scans of the burner running at this $X_{Kr} = 0$ condition were then obtained to measure $\bar{\mu}_B$. It is critical that these scans be taken with a hot burner if Eq. (4) is to be faithfully applied via background subtraction; specifically, the SiC porous disks undergo thermal expansion with temperature, and attempting to perform background subtraction between a hot burner scan and cold air scan was shown to result in poor image registration. Multiple scans are taken at each condition to ensure that noise levels of both $\bar{\mu}_M$ and $\bar{\mu}_B$ could be equally reduced via averaging over several trials. Finally, note that subtraction is purposely performed in reconstruction (attenuation) space rather than in projection (absorbance) space—while more computationally intensive, this procedure ensures faithful reconstruction of each acquisition and allows registration between reconstructed datasets (mostly based on solid body rotation) to be performed in physical space.

4. Data analysis methods

XCT reconstructions fundamentally give point measurements of $\bar{\mu}$ at each voxel. Attenuation measurements in voxels in the gas-phase sections at the top and bottom of the burner tube will reflect the difference between the burned and unburned gas mixture, while those in the porous media sections require more careful consideration. Specifically, pores in the 100 PPI and 65 PPI sections are typically smaller than the 200 μm reconstruction resolution, meaning that voxels in these domains effectively represent a volume-average of the solid and the gas. In fact, the volume fraction of each porous section can be extracted by computing the ratio $\Delta\bar{\mu}_{PM}/\Delta\bar{\mu}_{Kr}$ over a large number of voxels (with $\Delta\bar{\mu}_{PM}$ indicating the value obtained in the porous media and $\Delta\bar{\mu}_{Kr}$ that for pure krypton gas), as the ratio of these two attenuation differences will simply reflect the relative amount of krypton gas contained in each segment of the burner tube (i.e. the solid will subtract out, as its attenuation remains constant). This method gives gas volume fractions of 0.80 for the 100 PPI section, 0.85 for the 65 PPI section, and 0.93 for the 3 PPI section. Image processing is performed inside the 3 PPI section of the background measurement to isolate voxels containing the solid via thresholding and to subsequently extract all gas phase voxels to be used for evaluation of internal flame structure. Note that typical attenuation values are 0.5 cm⁻¹ for solid-phase SiC, 0.05 cm⁻¹ for air reconstructed inside the 3 PPI SiC pores, and 0.06 cm⁻¹ for ambient-temperature CH₄/Kr/N₂/O₂ gas mixture inside the 3 PPI SiC pores, meaning that this thresholding procedure is quite robust. The air attenuation value can be considered a constant offset that is eliminated via background subtraction, as air attenuation is physically negligible at these photon energies. Because we are interested in gas-phase attenuation changes that imply information about the thermodynamic state, attenuation differences in the 65 PPI and 100 PPI porous sections are scaled by the appropriate volume fraction to ensure accurate reflection of the gas-phase state. We will refer to data in which this adjustment has been made by using the superscript g to indicate that we are working with the attenuation only of the *gas phase*.

In the following analysis, an average over twenty air scans is subtracted from an average over twenty burning scans to compute $\Delta\bar{\mu}^g$ at each point in space after volume fraction adjustment. In addition to averaging in time, a $3 \times 3 \times 3$ median filter is applied in order to remove remaining white noise *only* when results are visualized. Note that such a box physically represents a volume of size $0.6 \times 0.6 \times 0.6$ mm³, a value that is substantially smaller than

the size of the pores in the 3 PPI section, which typically have diameters on the order of 5 mm. Additionally, after locating solid voxels via thresholding based on $\bar{\mu}_B$ magnitude, the solid voxel regions are dilated by two pixels in all directions to minimize the effect of partial volume artifacts and any scan-to-scan misregistration on the gas phase measurements.

Computations of an implied temperature field can be accomplished at both the pixel and mean levels using Eq. (4) in combination with known upstream temperature values. Specifically, by Eq. (4), the quantity $\Delta \bar{\mu}^g T$ must remain constant at any point in the gas phase under the assumption of constant P and X_{Kr}, which appear reasonable given that the gas is homogeneously mixed, that no entrainment occurs, and that the flame is statistically planar. Thus, utilizing spatially resolved attenuation measurements at each voxel, we can compute a "self-calibrated" temperature at each voxel as,

$$T = T_0 \frac{\Delta \bar{\mu}_0^g}{\Delta \bar{\mu}^g}, \tag{7}$$

where the inlet temperature is measured to be $T_0 = 302$ K and inlet attenuation μ_0 is taken to be the average value in the bottom domain of the burner (the transparent portion upstream of the insulation in Fig. 1(a)) where the gas is at ambient temperature.

5. Results and discussion

5.1. Flame structure analysis

At this point, it is useful to examine the internal PMB flame structure using the 3D XCT dataset, where we refer to the horizontal directions as x and y while taking z to be the vertical (axial) direction. In Fig. 2, we present cross-sectional planes of the subtracted attenuation field along the vertical axis of the burner for both the present experiment with $X_{Kr} = 0.375$ and a previous version of the same experiment run with $X_{Kr} = 0.820$ along with the same equivalence ratio and data processing procedures. As shown in Fig. 2, the $X_{Kr} = 0.820$ case clearly gives results with less noise, as implied by Eq. (6)—however, given our emphasis on performing measurements at practically relevant conditions that are most analogous to fuel-air combustion, we analyze the $X_{Kr} = 0.375$ results in the remainder of this paper.

Given that $\Delta \bar{\mu}^g \sim 1/T$ from Eq. (4), these results show that areas of lower temperature will be indicated by regions of higher attenuation (assuming constant pressure and X_{Kr}). One phenomenon that is immediately apparent is that a substantial preheating of the incoming gas occurs in the 65 PPI and 100 PPI porous sections, within which there exists a noticeable axial variation in the attenuation

field. This is, in effect, an observation of excess enthalpy combustion in three dimensions. The 65 PPI and 100 PPI SiC sections, which are composed of a highly conductive solid material, are transporting heat upstream to the incoming gas, which then expands and exhibits lowered attenuation. This effect is likely augmented by the low flow rate characteristic of this experiment, which results in relatively small convective heat transport away from the highly conductive upstream SiC pieces.

Further, one can observe that burning within the porous matrix is not axially homogeneous. As expected, the regions of highest temperature occur nearest to the 3 PPI - 65 PPI interface on the 3 PPI side of the burner in Fig. 2, but the degree of homogeneity in the radial and azimuthal directions is better visualized with the in-plane attenuation data shown in Fig. 3. As the axial coordinate z increases, we see that the gas in the bottom of the 100 PPI section shown in panel (A) is noticeably cooler than that in the more substantially preheated 65 PPI section shown in panel (B) throughout the radial and azimuthal domains. The temperature in the exhaust gas, in panel (C), is also well visualized, and is significantly cooler than the burning zone of panel (D). Comparison of panels (D)–(F) demonstrates variation in combustion behavior through the 3 PPI combustion zone. Specifically, near the interface, we observe distinct homogeneity in the attenuation field, indicative of relatively consistent combustion conditions within this slice of the burner. Additionally, an average temperature decrease (attenuation increase) is observed as we move to the downstream sections of the burner, where the attenuation field appears to become slightly less homogeneous. Finally, the development of noticeable spatial inhomogeneity observed in the downstream sections of the burner (such as in panels (E) and (F)) hints at the existence of interesting pore-scale heat transfer physics which may well have an effect on the fundamental operation of PMBs.

5.2. Comparison of implied temperature to 1D model and traditional measurements

Additional insight into the fundamental physics of this burner can be attained by comparing the implied temperature field from the self-calibration procedure described above to that obtained from a 1D volume-averaged computational model. To enable this study, the system at hand was modeled using the 1D reacting flow solver in the CANTERA software package [17]. The solver was modified to account for the solid matrix environment, incorporating volume-averaged governing equations and the corresponding effective transport parameters. The computational model is adapted from that reported in Barra et al. [5] for a two-section porous media burner. Conservation equations for mass, gas species, gas energy, and solid energy are solved, using a version of the detailed GRI 2.11 chemical
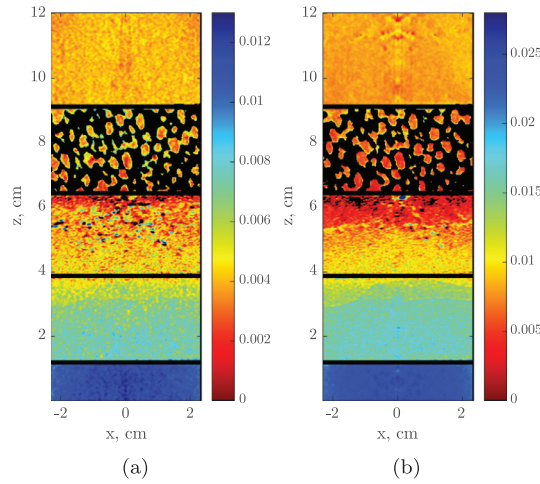
Fig. 2. Cross-sectional view of linear attenuation field, $\Delta\bar{\mu}^g$[cm^{-1}], for (a) $X_{Kr} = 0.375$ and (b) $X_{Kr} = 0.820$ (solid matrix in black); Black lines delineate the porous sections; Legends in panels (a) and (b) are scaled with krypton mole fraction. (color online)
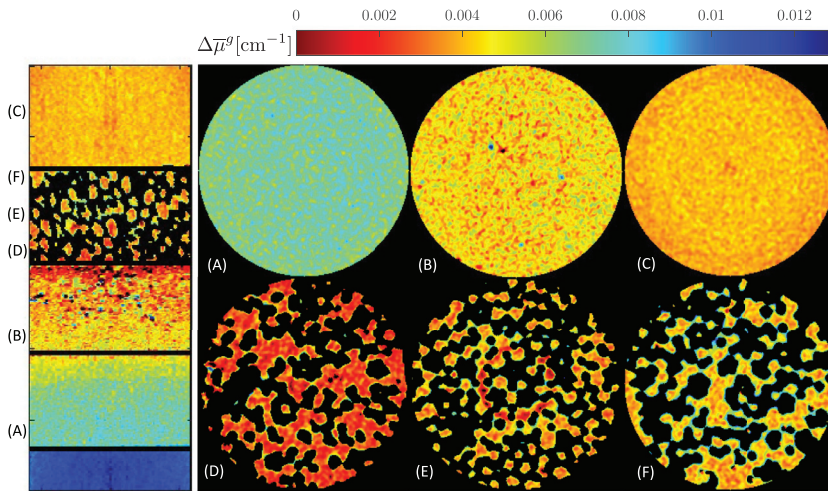

Fig. 3. Linear attenuation field $\Delta\bar{\mu}^g$ [cm^{-1}] at different sections through the burner (solid matrix in black); Heights are as follows with respect to the axis of Fig. 2–(A): 2.4 cm , (B): 4.4 cm, (C): 10.6 cm, (D): 6.5 cm, (E): 7.8 cm, (F): 9.1 cm; Locations are indicated on the vertical cross section. (color online)

mechanism for CH$_4$ combustion that has been augmented with krypton. Thermal non-equilibrium between the gas and the solid matrix is assumed and their interaction is modeled using a volumetric heat transfer coefficient appropriate for high-porosity ceramic foams [18]. We assume that the solid is inert and does not react with the gas mixture. Thermal conductivity and radiative heat extinction coefficient are estimated using an empirical model proposed by Hsu and Howell [19], while radiation coefficients are based on the experimental data of Henricks and Howell [20].

When using this 1D model to assess the performance of the XCT diagnostic, we average over all gas-phase voxels at each axial slice of the XCT dataset to reproduce the type of assumptions incorporated into the 1D model. We first obtain 1D attenuation curves by averaging $\Delta\bar{\mu}^g$ at each position in the axial direction for each reconstruction to give 1D cross-sectionally averaged $\Delta\bar{\mu}^g$ curves. Importantly, averaging over twenty scans ensures a reasonable level of statistical convergence in the results. This mean $\Delta\bar{\mu}^g(z)$ curve can be observed over the relevant axial domain in Fig. 4(a).
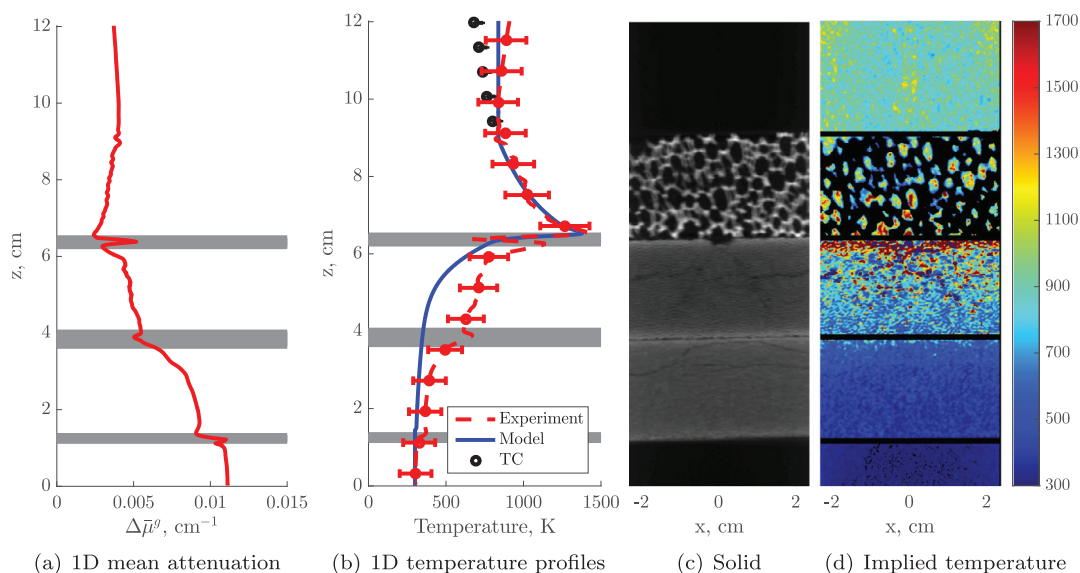
Fig. 4. (a) Mean attenuation curve $\Delta\bar{\mu}^g(z)$, [cm^{-1}]; (b) Comparison of 1D model to implied temperature results and thermocouple (TC) measurements; (c) Visualization of solid structure; (d) Vertical cross section of 3D implied temperature [K] field; Note that all subfigures are on the same z axis and black lines delineate the porous sections. (color online)

As shown in Fig. 4(b), 1D implied temperature calculated from the self-calibration procedure agrees well with both measured temperature in the unburned gas section and steady-state thermocouple data obtained in the burned gas section. Note that the thermocouple data has not undergone explicit correction for radiation loss; as discussed by Bradley and Matthews [21], radiation losses can result in thermocouple readings that are on the order of 10–50 K smaller than the actual gas temperature that would be recorded by XCT. Error bars on the thermocouple measurements reflect a 30 K radiation loss estimated as in [22]. Additionally, the X-ray measurements themselves are subject to some uncertainty—in the 1D comparison, we show error bars reflecting 95% confidence intervals that take into account both the expected standard error of the sample mean and detector drift [12] while incorporating a conservative 5% contribution to the coefficient of variation resultant both from minor X_{Kr} variation in the combustion zone and from small, spatially localized areas in the 65 PPI porous media where $\Delta\bar{\mu}^g$ attains unphysical values.

Overall, reasonable qualitative agreement with the model is observed in terms of flame position at the interface between the 3 PPI and 65 PPI burner sections, the overall temperature level within the burner, and the temperature pattern observed in the downstream portion of the burner. As discussed above, while the model predicts a flame exactly at the interface with minimal upstream conduction, the experiments explicitly suggest evidence of an extended preheat zone throughout the 65 PPI SiC

section, which is indicative of the level of internal heat exchange within the porous burner. This discrepancy is likely the result of a combination of insufficiencies in the interface transport processes in the 1D volume-averaged model, uncertainties in material properties, the steady-state nature of the 1D model, and spatial variations in the experimental porosity field. It is also possible that the discrete nature of the combustion wave in different segments of the porous media contributes to these differences. Further, note that there exist several sharp changes in the mean attenuation curve in Fig. 4(a) and the temperature curves in Fig. 4(b). Each of these appears to occur directly at the interface between two different burner segments, and likely results from imperfect registration and axial alignment of the porous sections at the interface combined with particularly low signal in the hottest portion of the burner. Thus, these sections of the plots have been grayed out to indicate areas where results are not necessarily reliable.

Several aspects of Fig. 4(c) and (d) bear further discussion. First, the vertical slice of the 3D implied temperature field yields better visualization of temperature variation than the attenuation map in Fig. 2 because we are plotting a quantity that is directly proportional to temperature. The axial extent of the flame zone is substantially more apparent from this data, which indicates that most of the combustion occurs within the bottom third of the 3 PPI burner section. This is consistent with the observed extent of the radiant flame zone visible through the ceramic fiber insulation between

the burner and quartz tube. It is important to note that while these 3D results are encouraging, further work on calibrating temperature to krypton tracer concentration would be helpful in lowering the level of uncertainty surrounding quantitative voxel-to-voxel subtracted measurements, which can be on the order of the measurement at the tail ends of the voxelwise $\Delta\bar{\mu}^g$ distribution. Thus, Fig. 4(d) is meant to give a first glance at the 3D temperature field, but should be viewed in light of experimental uncertainty at the individual voxel level, which is to a degree mitigated in visualization by the $3 \times 3 \times 3$ median filter described above. As a final comment, the solid visualization of Fig. 4(c) (a scan of the burner containing only air in the gas phase) shows that cracking has occurred in the upstream SiC porous foams over the course of these experiments. While such crack-detection represents a more traditional use of XCT, it is nonetheless useful in working with PMBs due to the fact that questions about potential inhomogeneities in internal flow patterns can be answered without destructive procedures.

6. Conclusions

This study has demonstrated the potential of XCT to provide relatively unique insight into internal processes characteristic of PMBs. In addition to allowing for qualitative assessment of internal flame structure, non-intrusive extraction of implied temperature fields from a multi-zone SiC PMB yields results that agree well with both 1D volume-averaged computational models and results from traditional thermocouple measurements. Further, the XCT method was able to distinguish the substantial, mostly homogeneous internal preheat zone in the 65 PPI SiC upstream section that was not captured by the 1D model and which would have been very difficult to diagnose using traditional methods.

The fact that PMB systems have relatively high thermal mass and tend to operate near a steady state condition appears to make them particularly amenable to XCT measurements. However, while XCT has a major strength in its ability to non-intrusively yield 3D field data, its temporal resolution is also hindered by the requirement of inter-scan averaging to achieve reliable measurements at contrast levels characteristic of radiodense gas-phase flows. Developing methods to improve signal-to-noise ratio and scan acquisition rate using a combination of hardware and software improvements (optimized reconstruction techniques, advanced detectors, brighter sources, etc.) would further enhance the attractiveness of this diagnostic tool. In addition, improving temporal resolution with a multiple-detector, multiple-source system that would allow XCT measurements to capture transient effects could be quite help-

ful in developing discrete models of porous media and filtration combustion. In the end, the experiment described here has demonstrated the viability of performing useful gas-phase combustion experiments within the limitations of XCT hardware, and suggests that this experimental method holds substantial promise in providing high-resolution 3D datasets describing implied gas-phase temperature and density fields within optically inaccessible environments.

Acknowledgments

References

[1] D. Trimis, F. Durst, *Combust. Sci. Technol.* 121 (1–6) (1996) 153–168.
[2] M.A. Mujeebu, M.Z. Abdullah, M.A. Bakar, A. Mohamad, R. Muhad, M. Abdullah, *J. Environ. Manag.* 90 (8) (2009) 2287–2312.
[3] V. Babkin, A. Korzhavin, V. Bunev, *Combust. Flame* 87 (2) (1991) 182–190.
[4] V. Khanna, R. Goel, J. Ellzey, *Combust. Sci. Technol.* 99 (1–3) (1994) 133–142.
[5] A.J. Barra, G. Diepvens, J.L. Ellzey, M.R. Henneke, *Combust. Flame* 134 (4) (2003) 369–379.
[6] A.J. Barra, J.L. Ellzey, *Combust. Flame* 137 (1) (2004) 230–241.
[7] M.T. Smucker, J.L. Ellzey, *Combust. Sci. Technol.* 176 (8) (2004) 1171–1189.
[8] J. Kiefer, M. Weikl, T. Seeger, F. Von Issendorff, F. Beyrau, A. Leipertz, *Proc. Combust. Inst.* 32 (2) (2009) 3123–3129.
[9] B. Stelzner, C. Keramiotis, S. Voss, M. Founti, D. Trimis, *Proc. Comb. Inst.* 35 (3) (2015) 3381–3388.
[10] J. Chaouki, F. Larachi, M.P. Dudukovic, *Ind. Eng. Chem. Res.* 36 (11) (1997) 4476–4503.
[11] M. Linne, *Prog. Energy Combust.* 39 (5) (2013) 403–440.
[12] J. Dunnmon, S. Sobhani, T.W. Kim, A. Kovscek, M. Ihme, *Exp. Fluids* 56 (2015) 193.
[13] A. Macovski, *Medical Imaging Systems*, Prentice Hall, 1983.
[14] J.T. Bushberg, J.A. Seibert, E.M. Leidholdt, J.M. Boone, *The Essential Physics of Medical Imaging*, third ed., Lippincott, Williams, and Wilkins, 2011.
[15] J. Hsieh, *Computed Tomography*, John Wiley and Sons, 2009.

[16] L. Feldkamp, L. Davis, J. Kress, *JOSA A* 1 (6) (1984) 612–619.

[17] D.G. Goodwin, in: CANTERA: An Open-source, Object-oriented Software Suite for Combustion, 1998.

[18] L. Younis, R. Viskanta, *Int. J. Heat Mass Transf.* 36 (6) (1993) 1425–1434.

[19] P. Hsu, J.R. Howell, *Exp. Heat Transf.* 5 (4) (1992) 293–313.

[20] T. Hendricks, J. Howell, *J. Heat Transf.* 118 (1) (1996) 79–87.

[21] D. Bradley, K. Matthews, *J. Mech. Eng. Sci.* 10 (4) (1968) 299–305.

[22] G.E. Glawe, F.S. Simmons, T.M. Stickney, Radiation and Recovery Corrections and Time Constants of Several Chromel-alumel Thermocouple Probes in High-temperature, High-velocity Gas Streams, *Technical Report*, Lewis Flight Propulsion Lab., Cleveland, 1956.